Cyclical geothermal unrest as a precursor to Iceland’s 2021 Fagradalsfjall eruption

Published Version:
Flóvenz, Ó.G., Wang, R., Hersir, G.P., Dahm, T., Hainzl, S., Vassileva, M., et al. (2022). Cyclical geothermal unrest as a precursor to Iceland’s 2021 Fagradalsfjall eruption. NATURE GEOSCIENCE, 15(5), 397-404 [10.1038/s41561-022-00930-5].

Availability:
This version is available at: https://hdl.handle.net/11585/897080 since: 2022-10-24

Published:
DOI: http://doi.org/10.1038/s41561-022-00930-5

Cyclical geothermal unrest as a precursor to Iceland's 2021 Fagradalsfjall eruption

Authors

Ólafur G. Flóvenz (1), Rongjiang Wang (2,3), Gylfi Páll Hersir (1), Torsten Dahm (2,4), Sebastian Hainzl (2), Magdalena Vassileva (2,5,9), Vincent Drouin (1, 10), Sebastian Heimann (2,4), Marius Paul Isken (2,4), Egill Á. Gudnason (1), Kristján Ágústsson (1), Thorbjörg Ágústsdóttir (1), Josef Horálek (6), Mahdi Motagh (2,5), Thomas R. Walter (2,4), Eleonora Rivalta (2,7), Philippe Jousset (2), Charlotte M. Krawczyk (2,8), Claus Milkereit (2)

1. ÍSOR, Iceland GeoSurvey, Reykjavik, Iceland

2. Helmholtz Centre Potsdam GFZ German Research Centre for Geosciences, Potsdam, Germany

3. Institute of Geophysics and Geomatics, China University of Geosciences, Wuhan 430074, China

4. University of Potsdam, Institute of Geosciences, Potsdam, Germany

5. Institute for Photogrammetry and GeoInformation, Leibniz University Hannover, 30167 Hannover, Germany

6. Institute of Geophysics, Czech Academy of Sciences Prague, Czech Republic

7. Department of Physics and Astronomy, University of Bologna, Italy

8. TU Berlin, Institute of Applied Geosciences, Germany

9. Leibniz University Hannover, Institute of Photogrammetry and GeoInformation

10. Icelandic Meteorological Office, Reykjavík, Iceland

Abstract

Understanding and constraining the source of geodetic deformation in volcanic areas is an important component of hazard assessment. Here, we analyse deformation and seismicity for one year prior to the March 2021 Fagradalsfjall eruption in Iceland. We generate a high-

resolution catalogue of 39,500 earthquakes using optical cable recordings and develop a poroelastic model to describe three pre-eruptional uplift and subsidence cycles at the Svartsengi geothermal field, 8 km west of the eruption site. We find the observed deformation is best explained by cyclic intrusions into a permeable aquifer by a fluid injected at 4 km depth below the geothermal field, with a total volume of 0.11±0.05 km^3 and a density of 850±350 kg/m^3. We therefore suggest that ingression of magmatic CO2 can explain the geodetic, gravity, and seismic data although some contribution of magma cannot be excluded. Our results demonstrate that inflation and deflation cycles with periods of several months over scales of tens of square kilometres commonly observed in volcanic systems around the world can be caused by the migration of deep magmatic fluids and gases into upper crustal hydrothermal systems. It highlights the interaction of volcanic processes and the behaviour of geothermal systems to address hazard assessments.

Recent volcanic and seismic unrest with surface deformation at the Reykjanes Peninsula (RP) plate boundary in SW Iceland, in and around the Svartsengi high-temperature (HT) field (**Fig. 1**), reveals a previously unexplored cyclic interaction between tectonic spreading, magmatic reservoirs, and supercritical magmatic fluids interacting with hydrothermal reservoirs.

On January 22nd, 2020, an earthquake swarm started 3 km east of Svartsengi. Simultaneously, uplift was recorded at the geothermal field close to the re-injection site[1] of the power plant, followed by subsidence. Three such cycles of inflation and deflation occurred until July 2020, where each inflation was followed by continuous deflation and diminishing seismicity (**Fig. 2c**). Similar inflation started in August 2020 at the centre of the Krýsuvík HT field, 20 km east of Svartsengi (**Fig. 1**). In February 2021, crustal extension and an intense earthquake swarm revealed the formation of a NE striking magmatic dyke between the two HT fields, followed by the Fagradalsfjall eruption 8 km east of Svartsengi on March 19th, 2021. The spreading axis of the Mid-Atlantic Ridge comes on land at the SW corner of the RP. There, it bends into a 60 km long N70°E striking oblique plate boundary, expressed by a 5-10 km wide seismic and volcanic zone, where large episodic earthquake swarms occur every 20-40 years[2] with magnitudes up to M6, mostly on N-S trending strike-slip faults. Volcanic eruptions have occurred at intervals of 800-1000 years during the past 4000 years, the last one ending in 1240 AD[3]. Each volcanic episode might last for 1-3 centuries with basaltic lava flows from N45°E trending fissures extending into the adjacent plates[4]. HT geothermal fields with reservoir temperature of 240-330°C at 1-3 km depth[5] have formed at the intersection of the seismic zone and the main volcanic fissure swarms (**Fig. 1**). One well, IDDP-2 at the Reykjanes HT field (**Fig.1**), was drilled to 4.6 km depth[6] close to the brittle-ductile transition (BDT) where bottom hole temperature is estimated to be about 600°C[7] just beneath a hydrostatic pressurized aquifer (~35 MPa). Corresponding results were obtained in the IDDP-1 well at the Krafla HT field in North Iceland. The crust above the aquifers is in both cases fully elastic and the fluid pressure in the rock is hydrostatic down to the BDT.

The upper crust of the RP is approximately 4.5 km thick[8,9,10] and composed of basaltic extrusives with a downward increasing alteration and a higher proportion of intrusives. The lower crust down to Moho at ~15 km depth is thought to be made of intrusives with no evidence of melt[10,11,12]. The BDT is generally at 6-7 km depth beneath the RP, rising up to 4-5 km depth below the HT fields[13,14,15] with an estimated temperature of ~600°C[1,7,16,17].

The 76 MW_e power plant at the Svartsengi HT field and the Blue Lagoon Spa (**Ext. data Fig. 1**) are the heart of the Geothermal Resource Park, providing electricity and hot and cold water to 25,000 residents and local industries[18]. The average annual production rate is about 0.45 m^3/s, of which about 0.3 m^3/s are re-injected into the reservoir. These re-injection rates are an order of magnitude smaller than the rates needed to explain the observed uplift in 2020.

The cyclic deformation and earthquake activity at two distinct HT fields at the RP plate boundary and the time lag prior to a distant fissure eruption is unusual and was previously not observed. Using a comprehensive modelling approach, we show that the ascent of magma-derived volatiles into a sealed aquifer above the BDT beneath the Svartsengi HT field can explain the uplift and subsidence cycles, and can be interpreted as a precursor to a coming eruption.

Transient deformation at the Svartsengi HT field

Analysis of twelve months of satellite InSAR time-series data supported by GNSS data (see methods), processed in both ascending and descending configuration, reveals an elliptical area exceeding 80 km² affected by uplift and subsidence at Svartsengi, along with minor horizontal displacements (**Fig. 2a & Ext. data Fig. 2**). The major axis of the elliptical area is ~12 km long, striking N60°E and the perpendicular axis is 8.5 km long. The major axis follows the dominant strike of the geothermal reservoir (**Ext. data Fig. 1**) but deviates both from the N45°E strike of volcanic fissures and the N to NE trending strike-slip faults mapped at the surface on the RP.

The duration of successive uplift episodes increased while the uplift rate decreased correspondingly (**Ext. data Fig. 3**). The first episode had the highest uplift rate of 2.2 mm/day and a total uplift of 66 mm over 30 days (**Fig. 2b**). It was followed by 18 days of subsidence, totalling less than 10 mm. The second episode had an uplift rate of 1.1 mm/day and a total uplift of 55 mm over 48 days. It was followed by a faster subsidence episode lasting approximately 24 days, with a total subsidence of 16 mm. The final episode, with an uplift rate of 0.5 mm/day, produced a total uplift of 32 mm over 60 days. On July 18th, an earthquake of magnitude M4.1 occurred near the inflation centre[19] (**Ext. data Fig. 1**). It was followed by a period of subsidence visible on InSAR until mid-December with an average subsidence rate of 0.2 mm/day and a total subsidence of 38 mm. The cumulative uplift observed at the centre of displacement was slightly less than 150 mm and by December 2020 the actual uplift was reduced to 90 mm.

Free-air gravity changes

Gravity provides additional insights, as changes in gravity depend on the mass of the intruded fluids, while deformation depends on volume change. We measured gravity in four consecutive campaigns (**Tab. S1**) at 10-12 existing permanent stations along an L-shaped profile extending north and west from the centre of uplift (**Ext. data Fig. 4**).

The first campaign was conducted a week after the start of the first uplift episode and repeated shortly after the end of the second one. Measured gravity changes between the first and second campaign show a consistent free-air corrected gravity increase of 10-14 μGal around the centre of uplift (**Ext. data Fig. 5 & Tab. S1**). A consistent free-air corrected gravity decrease of 4-8 μGal is observed at the uplift centre from April to October, during the third uplift episode and the following deflation. Between October 2020 and February 2021, the free-air corrected gravity decrease continues at most stations. The maximum decrease averaged over the three closest stations to the centre of uplift was 5 μGal.

To estimate the cumulative gravity increase, we need to account for the gravity changes during the first week and during the third uplift episode that were not directly covered by the gravity campaigns. This is done by assuming the same ratio of gravity increase to the uplift at the inflation centre (170 μGal/m) as measured during the first two uplift episodes. In addition, we corrected for the long-term background gravity decrease caused by the geothermal production. The resulting cumulative gravity increase of all three inflation episodes equals to

27 μGal at the centre of uplift. However, 13 months after the start of the unrest period, the corrected net free-air gravity change was reduced to 14 μGal, implying that almost half of the intruded mass had disappeared or migrated away from the inflation centre.

Seismicity

To evaluate the background seismicity and the rate changes during the transient deformation, we used the national catalogue[20] of the Iceland Met Office (IMO). For a more detailed analysis of the spatiotemporal patterns during the unrest period, we created a new catalogue for the year 2020, using 26 seismic stations spaced up to 30 km around Svartsengi. For the first time, we integrated distributed acoustic sensing (DAS) data from a 21-km-long fibre optic telecommunication cable buried 80-90 cm below the ground from the southern tip of Reykjanes to Grindavík, crossing the Svartsengi HT field[21] (**Ext. data Fig. 4**). To detect and locate the smallest earthquakes, we modified a waveform stacking and migration method[22] to combine seismic and continuous DAS data. The new and more complete catalogue covers the period from February 1st to August 30th. We detected 39,500 earthquakes with magnitudes of M>-1, i.e., a factor of 1.9 more events, and localised the majority automatically. The locations have high quality, both laterally and vertically, since sensors and DAS cable were located directly above the uplift zone, and the azimuthal distribution of all stations was unusually good.

Seismicity shallower than 4 km depth occurs mainly within the elliptical uplift region, with the shallowest events at the centre of uplift (**Fig. 3b & Ext. data Fig. 6**). This suggests that many of these earthquakes are triggered by elastic bending stresses in the roof above the aquifer. . The absence of earthquakes deeper than 4 km depth at the uplift centre supports the hypothesis of an updoming BDT rising from 6-7 km depth (**Fig. 3**).

Models of pre-eruptive processes

The deformation pattern suggests an inflation source at depth. We first tested an isotropic point-source (Mogi) model[23,24] to retrieve information about the source location, depth and strength. For the three uplift episodes, the best fitting parameters from inversion of the InSAR data results in source depths ranging from 4.0 to 4.9 km with horizontal location difference within 330 m. The inferred volume changes are estimated to be 4.70, 3.55 and $2.75 \cdot 10^6$ m^3, respectively, and cumulatively explain over 90% of the observed deformation (**Suppl. Information Figs. S1, S2 & Tab. S4**).

To better match the elliptical shape of the uplift pattern, we also tested rectangular dislocation models[25]. The uplift episodes can be modelled by three 10 m thick, 7-9 km long and 30-50 m wide nearly horizontal intrusions at a depth between 3.7-4.4 km, with an average strike of N60°E. However, the subsidence rate after each uplift episode seems too fast and large (**Fig. 2c**) to be explained by a cooling-related volume reduction of a magma intrusion. Similarly, it is difficult to explain the significant decrease of the free-air gravity observed in the central area following the uplift episodes. Furthermore, the induced change in Coulomb failure stress is concentrated directly around the presumed magma body and therefore cannot explain the triggered seismicity, which has been observed over a wider area (**Fig. 4**). Anomalously low Vp/Vs ratios are also observed in the lower crust beneath Svartsengi[26,27], indicating gas-saturated porous rocks rather than partial melt. Analysis of ambient seismic noise prior to the unrest[28] indicates a drop in S-wave velocities beneath Svartsengi, while a 1% temporary drop in seismic velocities is also reported during the unrest period at Svartsengi[29]. In both cases, the observations can be explained by spatial or temporary changes in crack density without a need for magma involvement.

As an alternative, we employ a poroelastic model considering a strongly coupled diffusion and deformation process[30]. The domain consists of a thin, permeable, porous aquifer layer at a depth of approximately 4 km, embedded in a multi-layered poroelastic half-space (**Ext. data Fig. 7**). The elastic parameters are adopted from the seismic reference model used for earthquake locations (**Suppl. Information Tab. S3**). During the three uplift episodes, the aquifer is pressurized by a fluid intrusion (injection) along a N60°E trending line source with the strength of the fluid intrusion modelled by a Gaussian distribution with a standard deviation of 2 km We inverted the InSAR data for the 12-months period of unrest, with fluid inflow during uplift and no inflow during subsidence (**Fig. 5b**). The resulting intrusion rates depend on the Skempton coefficient (B) used to describe how much of intruded fluid can be accommodated by the aquifer through a given pressurization. The smaller B, the more the intruded fluid volume. Based on previous interdisciplinary observations including realistic estimate of temperature, pressure and porosity within the aquifer, we estimate $0.08 \leq B \leq 0.19$ as a realistic variation range for the assumed aquifer. Uncertainties in other parameters on the volume and density estimations are negligible compared to the effect of the uncertainty in the Skempton coefficient. (**Suppl. Information sheet IS3**). Accordingly, the total intrusion volume can be estimated realistically to be 0.07- 0.16 km^3.

The fluid intrusion causes poroelastic response resulting in surface deformation, fluid flow in the aquifer, and the Coulomb stress changes on the fault planes. It explains the InSAR time series, particularly the rapid subsidence following each cyclic uplift, the free-air gravity changes and the seismicity variations in time and space.

The total mass of the intruded fluid, which best fits the campaign gravity data (**Fig. 2d and Ext. data Fig. 5**), is about 82 Mt. It yields a fluid density in the range of 500-1200 kg/m^3. We estimate the range of pressure and temperature within the aquifer to be $110 < P < 150$ MPa and $350 < T < 600$°C. These values imply that the intruded fluid could be water (≤ 670 kg/m^3), carbon dioxide (≤ 740 kg/m^3), supercritical sulfur dioxide, or a mixture of gas and magma (2700 kg/m^3) with maximum 33% volume ratio of the magma (**Suppl. Information sheet IS3**).

Although re-injection of fluid from the power plant might comply with the density value, the re-injection rates are far too small to explain the observed volume and gravity change. Since both H_2O and SO_2 remain dissolved in magma until close to the surface[31], carbon dioxide is practically the only possible fluid candidate. Therefore, we conclude that the injected fluid is either pure CO_2 or in a CO_2 mixture with up to 33% magma volume.

The poroelastic model also explains the seismic rate changes relative to the background activity. Specifically, we analysed the seismicity rate changes during the deformation, relative to the average background rate between the years 2000 and 2020 in the region surrounding the deformation centre. The observed seismicity rate changes were compared to those predicted by a rate-and-state friction response[32] based on the Coulomb failure stress changes calculated from the poroelastic aquifer model. The predicted seismicity changes (**Fig. 4**) are in good agreement with the observed spatiotemporal earthquake patterns, providing further evidence for the poroelastic aquifer model.

We propose a feeder channel model that is consistent with the results from the poroelastic model and fits the time scales of uplift and subsidence (**Fig. 5 & 6**). Finally, we propose a conceptual model supported by geochemical observations of the erupted basaltic lava in Fagradalsfjall (**Suppl. Information sheet IS2**).

It incorporates a magmatic reservoir containing crystal mush at 15-20 km depth, fed by slowly upwelling currents of mantle derived magma (**Fig. 6 & Information sheet IS2**). We propose that volatiles released from inflowing enriched magma into the sub-Moho reservoir migrated upwards, possibly in fluid plumes modelled to explain the formation of porphyry-copper ore shells[33]. The volatiles were possibly trapped for weeks or months at the impermeable BDT at ~7 km depth beneath Fagradalsfjall, generating overpressure, but not high enough to lift the overburden (~220 MPa) and cause surface deformation. This might have triggered the earthquake swarms that occurred within the brittle crust beneath Fagradalsfjall in 2017[34] and late 2019. After reaching a certain limiting overpressure at the top of the fluid column, i.e., when a certain volume has accumulated, the magmatic volatiles were diverted upwards, just below the BDT. The formed channel was episodically used by lithostatic pressurized fluid batches to migrate toward the hydrostatic pressurized aquifer (~ 40 MPa) at 4 km depth at the bottom of the convective HT field. They passed through the BDT and increased the pressure sufficiently (>110 MPa) to cause the uplift.

The feeder channel model for the lower crust explains episodic inflow with exponentially decreasing intensity and increasing recurrence times. Exponential decay is expected for pressure-driven draining from a deep reservoir with finite volume[35] (see method section and **Suppl. Information sheet IS1**). Episodic transport of fluid (CO_2) batches indicates a valve mechanism in the channel, controlled e.g., by pressure-dependent permeability fluctuations[36] or strength/fracture toughness threshold mechanics[37]. For B = 0.12, as an example, the three constant intrusion rates would have been 17.1, 8.9 and 5.1 m^3/s, respectively, yielding a total intrusive volume of about 0.11 km^3 (**Fig. 4b**). For smaller or larger B values, the intrusion rates and volume can be scaled correspondingly. We infer that the first three fluid batches were directed to the Svartsengi HT field, but that the fourth one in August was directed to the Krýsuvík HT field where similar geothermal conditions are expected (**Fig. 6 & Ext. data Fig. 8**). Finally, in February 2021, the overpressure led to the fracturing of the brittle crust, forming an ~8 km long magmatic dyke that ended with the Fagradalsfjall eruption in March.

Our model is consistent with the initial behaviour of the eruption that started March 19th, 2021. In contrast to the violent initial phase of eruptions derived from a magma chamber, the eruption rate was gentle during the first month. After that, it substantially increased with an average production rate close to 11 m^3/s based on the lava volume deposited at the surface[38]. Accounting for the porosity of the lava, it could correspond to 8-9 m^3/s of magma outflow. In our conceptual model, the volatiles from the degassing magma reservoir had already detached from the initial magma batch prior to the eruption, rising from the upper mantle and trapped at the BDT, where it eventually forced a different path through the ductile part of the crust to the underpressurized geothermal reservoirs at the BDT. From the total mass of CO_2 injected into the roots of the HT fields, we can estimate that the minimum volume of degassed magma beneath the present eruption site is at least of the order of 2-9 km^3 (**Fig. 6 & Suppl. Information sheet IS2**). Consequently, the available volume of magma is neither a limiting factor for the longevity of the eruption nor the erupted volume.

This model helps to explain the role and importance of HT geothermal fields in the complicated mechanism leading to volcanic eruptions.

Acknowledgements

The authors are grateful to all those who assisted to generate this article including Halldór Geirsson, University of Iceland, for providing the time series of a permanent GNSS station, allowing us to control InSAR data, Ingvar Þór Magnússon for collecting and processing the gravity data, Þorvaldur Þórðarson, University of Iceland and Alex Hobé, Uppsala University, for useful discussions, Enikõ Bali and Guðmundur H. Guðfinnsson, University of Iceland, for valuable assistance with the geochemical calculations, Mila Telecommunication Company for access to the fiber optic cable, Iceland Met Office for the access to the earthquake catalogue, seismic waveforms and GNSS stations and Christopher Wollin, Kemal Erbas and Thomas Reinsch for DAS assistance. The field work of GFZ was part of a HART rapid response activity funded by GFZ. DEM(s) were created from DigitalGlobe, Inc., imagery and funded under National Science Foundation awards 1043681, 1559691, and 1542736. The work of Marius Isken

was supported by the DEEPEN project (BMWI 03EE4018).

Author contributions statement:

ÓGF Co-ordination, writing, analysis of gravity, seismic and geothermal data, modelling concepts.

RW Numerical and theoretical modelling, development of porous media deformation approach and gravity modelling.

GPH Gravity measurements, data acquisition DAS, field work management.

TD Coordination, writing, modelling concepts, analytical model of cyclic channel flow.

SH1 Statistical analysis and modelling of seismicity.

MV Analysis of InSAR data, Mogi model inversion.

VD Analysis of InSAR data.

SH2 DAS processing, development of the Lassie stacking approach, automatic earthquake detection/location for the combined network.

MI DAS data conversion and processing, earthquake detection/location, code development.

EÁG Seismicity analysis, incl. focal mechanisms, data acquisition DAS, manual location of earthquakes from the enlarged network.

KÁ Seismicity analysis, seismic network, contribution to field activity.

ThÁ Seismicity analysis, incl. focal mechanisms.

JH Contributed data from Czech temporary network.

MM Supervision and quality control InSAR analysis at GFZ.

TW Coordination InSAR analysis, contribution to manuscript drafting and writing.

ER Contribution to manuscript review, internal review of channel flow and fluid transport models.

PJ Concept DAS measurements and coordination DAS data acquisition, coordination of fieldwork in MAGIC at GFZ.

CMK Support of MAGIC HART initiative at GFZ, coordination of DAS data processing and storage, manuscript review.

CM Installed temp. seismic stations, field work coordination, conversion of seismic data, coordination of analysis and writing team at GFZ.

Competing interest statement

The authors declare no competing interests

Figure legends

Figure 1. Overview of the tectonics and seismicity of the Reykjanes Peninsula. The red and black fault lines denote postglacial volcanic eruption fissures and opening fissures, respectively. Yellow dots show the seismicity from September 2019 – May 2021. Yellow lines show the extent of the high temperature geothermal fields on the peninsula, according to resistivity measurements[1]. Only the Reykjanes and Svartsengi geothermal fields are currently operated. The blue stars show the centres of uplift in Svartsengi and Krýsuvík and the red star the 2021 eruption site at Fagradalsfjall. The dashed green line shows the NE-striking magmatic dyke intrusion, based on InSAR analysis and seismicity. Main roads are in black, and topography is indicated as coloured background. Main landmarks referenced in the text are shown on the map.

Figure 2. Results from the poroelastic model. **a.** Map of maximum cumulative uplift from January 6th to July 17th, 2020 (Day 192). The colour map shows the vertical component calculated by combining the ascending and descending LOS displacements, in comparison with the predicted uplift (dashed contour lines) based on the poroelastic model for the same time period. The GNSS time series from the station marked by the white with black dot circle

was used for the InSAR validation. The centre of uplift is obtained from the Mogi source inversion. The dashed line shows the cross-section profile in Fig. 3a. The location of the current Fagradalsfjall eruption is shown as a red triangle. **b.** Temporal snapshots of surface uplift derived from the InSAR data, compared with the model predictions. The double model curves for each snapshot show the values along the major and minor axes of the elliptic uplift pattern. **c**. Comparison of the predicted and measured ascending and descending LOS displacements at the pixel nearest to the uplift centre. The gray bars show the observed seismicity rates within 5 km distance from the centre. **d.** Free-air gravity anomalies (blue diamonds) from campaign measurements between January 27^{th} and April 20^{th}, 2020, compared with the model predictions (solid curves) along the major and minor axes of the elliptic uplift pattern. Estimated error is ±5 μGal.

Figure 3. Sketch of fluid migration paths and aquifer location compared to observed seismicity and uplift. **a.** Maximum uplift (solid black line) and topography (dashed gray line) along the profile in Fig. 2a (x=0 at Mt. Thorbjörn). **b.** Density of micro-earthquakes between February and August 2020 (gridded file and colour scale) estimated in a 1 km wide band along the profile. The inferred brittle-ductile transition is indicated by the red dashed line. The manually relocated, largest events from the earthquake swarms from November (green circles) and December 2019 (gray circles) and at the beginning of unrest at Svartsengi (blue circles) are shown. The position and source intensity of the aquifer model are indicated.

Figure 4. Comparison of observed M≥1 seismicity (grey/black) with model predictions (coloured) based on induced crustal stress changes related to the geodetically inverted source model.

a. Histogram of earthquake numbers in the first 250 days of 2020 as a function of longitude. **b**. Map showing the model numbers of predicted earthquakes per km^2 as contour lines, while points indicate the observed events for the same period. Seismic stations are marked with triangles (blue = stations of the national seismic network in Iceland (SIL) operated by IMO, yellow = temporary network deployed by GFZ, green = seismic network operated by the Czech Academy of Sciences together with ÍSOR, pink = joint ÍSOR-IMO stations, and the DAS cable with a bold, blue line). **c**. Corresponding histogram of cumulative numbers as a function of latitude. **d**. Time-versus-longitude plot comparing the temporal evolution, where colours refer to the model's event density and magnitude-scaled points to observed earthquakes. **e**. Temporal evolution of the spatially integrated numbers, where stars mark the occurrence times of the three largest earthquakes.

Figure 5. Cyclic fluid transport model. **a.** Sketch of the deep geodynamic structures and the assumed magmatic and fluid reservoir discontinuously pressurizing the aquifer at 4 km depth. See the methods section for description of parameters and additional explanation. **b.** Model flow rate (red line) at entry point of transport channel to explain the time, duration, and magnitude of injections at the aquifer level (black rectangles). **c.** Time function of the predicted cumulative volume (red solid line) at the entry point of the discontinuous transport channel / fault is compared to the discontinuous volumes (black line) arriving at the aquifer level at 4 km depth. Red squares indicate the onset of the new batches of magmatic fluids. The open squares indicate the batch arriving at the Krýsuvík HT field in August 2020.

Figure. 6. A conceptual model of the processes leading to the uplift, gravity changes, seismic unrest, and the volcanic eruption. The model connects the datasets observed and the dynamic processes through modelling with mathematical and physical approaches.

Magmatic volatiles, mainly CO_2, and possibly magma migrate upwards from a magma reservoir containing crystal mush at 15-20 km depth, or just beneath Moho. When the gas pressure or volume has reached a critical value at the BDT, batches of gas are driven just below the BDT towards the hydrostatic pressurized geothermal aquifers where the gas intrudes and inflates the overburden. The process resembles those described by Fourier in 1999[56]. In February 2021, the pressure at the BDT managed to cause enough deviatoric stress to break through the brittle crust, forming a magmatic dyke intrusion and finally the eruption. The suggested amount of magma within the magma reservoir is based on the degassing process (Information sheet IS2). Vertical and horizontal scales are the same.

References

1. Flóvenz, Ó.G. et al. The interaction of the plate boundary movement in 2020 and exploitation of geothermal fields on the Reykjanes peninsula, Iceland. *Proceedings of the World Geothermal Congress 2020+1* (2021).
2. Björnsson, S., Einarsson, P., Hjartardóttir, Á.R. & Tulinius, H. Seismicity of the Reykjanes peninsula 1971 – 1976. *J. Volcanol. Geotherm. Res.* **391,** 106369 (2020).
3. Sæmundsson, K. & Sigurgeirsson, M.Á. Reykjanesskagi. In Sólnes J. et al. (ed), Náttúruvá á Íslandi, *Viðlagatrygging Íslands/Háskólaútgáfan*, 379—401 (2013).
4. Sæmundsson, K., Jóhannesson, H., Hjartarson, Á., Kristinsson, S.G. & Sigurgeirsson, M.Á. Geological map of Southwest Iceland, 1:100.000. *Iceland GeoSurvey* (2010).
5. De Freitas, M.A. Numerical modelling of subsidence in geothermal reservoirs: Case study of the Svartsengi Geothermal System, SW-Iceland. *MSc thesis, University of Iceland*, ISBN 978-9979-68-486-2 (2018).
6. Friðleifsson, G.Ó. et al. The Iceland deep drilling project at Reykjanes: Drilling into the root zone of a black smoker analog. *J. Volcanol. Geotherm. Res.* **391,** 106435, https://doi.org/10.1016/j.jvolgeores.2018.08.013 (2020).

7. Bali, E. et al. Geothermal energy and ore-forming potential of 600 °C mid-ocean-ridge hydrothermal fluids. *Geology*, **48**, https://doi.org/10.1130/G47791.1 (2020).

8. Pálmason, G. Crustal structure of Iceland. *Soc. Sci. Isl., Reykjavik, Iceland*, **XL** (1971).

9. Flóvenz, Ó.G. Seismic structure of the Icelandic crust above layer three and the relation between body wave velocity and the alteration of the basaltic crust, *J. Geophys*., **47**, 211–220 (1980).

10. Weir, N.R.W. et al. Crustal structure of the northern Reykjanes ridge and the Reykjanes peninsula, southwest Iceland. *J. Geophys. Res*., **106**, 6347-6368 (2001).

11. Hersir, G.P., Árnason, K. & Vilhjálmsson, A.M. Krýsuvík high temperature geothermal area in SW Iceland: Geological setting and 3D inversion of magnetotelluric (MT) resistivity data. *J. Volcanol. Geotherm. Res*. **391,** 106500, https://doi.org/10.1016/j.jvolgeores.2018.11.021 (2020).

12. Karlsdóttir, R., Vilhjálmsson, A.M. & Gudnason, E.Á. Three dimensional inversion of magnetotelluric (MT) resistivity data from Reykjanes high temperature field in SW Iceland. *J. Volcanol. Geotherm. Res*. **391,** 106498, https://doi.org/10.1016/j.jvolgeores.2018.11.019 (2020).

13. Blanck, H., Jousset P., Hersir, G.P., Ágústsson, K. & Flóvenz, Ó.G. Analysis of 2014–2015 on- and off-shore passive seismic data on the Reykjanes peninsula, SW Iceland. *J. Volcanol. Geotherm. Res.* **391**, 106548, https://doi.org/10.1016/j.jvolgeores.2019.02.001 (2020).

14. Kristjánsdóttir, S. Microseismicity in the Krýsuvík geothermal field, SW Iceland, from May to October 2009, *M.Sc. thesis, Faculty of Earth Sciences, University of Iceland*, (2013).

15. Gudnason, E.Á. et al. Seismic monitoring during drilling and stimulation of well RN-15/IDDP-2 in Reykjanes, SW-Iceland. *Proceedings of the World Geothermal Congress 2020+1* (2021).

16. Ágústsson, K. & Flóvenz, Ó.G. The Thickness of the seismogenic crust in Iceland and its implications for geothermal systems. *Proceedings of the World Geothermal Congress 2005* (2005).

17. Violay, M. et al. An experimental study of the brittle-ductile transition of basalt at oceanic crust pressure and temperature conditions. *J. Geophys. Res.*: *Solid Earth*, **117**(**B3**) (2012).
18. Albertsson, A. & Jónsson J. The Svartsengi resource park. *Proceedings of the World Geothermal Congress 2010* (2010).
19. Icelandic Meteorological Office. https://skjalftalisa.vedur.is
20. Böðvarsson, R., Rögnvaldsson, S.T., Slunga, R., & Kjartansson, E. The SIL data acquisition system at present and beyond year 2000. *Phys. Earth Planet. Inter*., **113**, 89–101 (1999).
21. Jousset, P. et al. Dynamic strain determination using fibre-optic cables allows imaging of seismological and structural features. *Nature Communications*, DOI: 10.1038/s41467-018-04860-y (2018).
22. López-Comino, J.A. et al. Characterization of Hydraulic Fractures Growth During the Aspo Hard Rock Laboratory Experiment (Sweden). *Rock Mechanics and Rock Engineering*, **50**, 11, 298-3001 (2017).
23. Mogi, K. Relations between the eruptions of various volcanoes and the deformation of ground surfaces around them. *Bull. Earthquake Res.Inst*. University of Tokyo, **36**, 99-134 (1958).
24. Lisowski, M. Analytical volcano deformation source models. In: *Volcano Deformation*. Springer Praxis Book, Berlin, Heidelberg. 279-304, 10.1007/7978-3-540-49302-0_8 (2007).
25. Okada, Y. Surface deformation to shear and tensile faults in a halfspace. *Bull. Seism. Soc. Am.*, **75** (1985).
26. Geoffroy, L., & Dorbath, C. Deep downward fluid percolation driven by localized crust dilatation in Iceland. *Geophys. Res. Lett*. **35**, 117302, doi:10.1029/2008GL034514 (2008).
27. Hobé, A., Gudmundsson, O., Tryggvason, A. & the SIL seismological group: Imaging the 2010-2011 inflationary source at Krýsuvík, SW Iceland, using time-dependent Vp/Vs tomography. *Proceedings of the World Geothermal Congress 2020+1* (2021).

28. Martins, J.E. et al. 3D S-wave velocity imaging of Reykjanes Peninsula high-enthalpy geothermal fields with ambient-noise tomography. *J. Volcanol. Geotherm. Res*., **391**, 106685, https://doi.org/10.1016/j.jvolgeores.2019.106685 (2020).

29. Cubuk-Sabuncu, Y. et al. Temporal Seismic Velocity Changes During the 2020 Rapid Inflation at Mt. Þorbjörn-Svartsengi, Iceland, Using Seismic Ambient Noise. *Geophys. Res. Lett.*, e2020GL092265, **48** https://doi.org/10.1029/2020GL092265 (2021).

30. Wang, R.A. & Kuempel, H.J. Efficient modelling of strongly coupled, slow deformation processes in a multilayered half-space. *Geophysics*, **68**, 705-717 (2003).

31. Sigmundsson, F. et al. Unexpected large eruptions from buoyant magma bodies within viscoelastic crust. *Nat. Commun.* **11**, 2403, https://doi.org/10.1038/s41467-020-16054-6 (2020).

32. Dieterich, J.H. A constitutive law for rate of earthquake production and its applications to earthquake clustering. *J. Geophys. Res*. **99**, 2601- 2618 (1994).

33. Weis, P., Driesner, T. & Heinrich, C.A. Porphyry-Copper ore Shells Form at Stable Pressure-Temperature Fronts Within Dynamic Fluid Plumes. *Science*, **338** (6114) 10.1126/science.1225009 (2012).

34. Hrubcová, P., Doubravová, J. & Vavryčuk, V., Non-double-couple earthquakes in 2017 swarm in Reykjanes Peninsula, SW Iceland: Sensitive indicator of volcano-tectonic movements at slow-spreading rift. *Earth and Planetary Science Letters*, **563,** p.116875, (2021).

35. Gudmundsson M.T. et al. Gradual caldera collapse at Bárdarbunga volcano, Iceland, regulated by lateral magma outflow. *Science*, **353** (6926), doi:10.1126/science.aaf8988 (2016).

36. Kennedy, B. et al. Pressure Controlled Permeability in a Conduit Filled with Fractured Hydrothermal Breccia Reconstructed from Ballistics from Whakaari (White Island), New Zealand*. Geosciences,* **10***, 138, 10.3390/geosciences10040138* (2020).

37. Sibson, R.H. Preparation zones for large crustal earthquakes consequent on fault-valve action. *Earth, Planets and Space*, https://doi.org/10.1186/s40623-020-01153-x (2020).

38. http://jardvis.hi.is/eldgos_i_fagradalsfjalli

Methods

InSAR data processing

We exploited the Copernicus Sentinel-1A and 1B satellite SAR data, which are available over Iceland in ascending (08/01/-15/12/2020) and descending (06/01/-13/12/2020) orbits with a revisit time of 6 days for each track. By calculating a single interferogram for the cumulative period between 20/01/-17/07/2020, we found four fringes in both geometries, representing a shift of approximately 11 cm in the line of sight (LOS) direction (**Ext. data Fig. 2**). A more detailed InSAR time series analysis shows three inflation and deflation episodes (**Ext. data Fig. 3**): first uplift 19/01/-18/02/2020, second uplift 07/03/-24/04/2020, and third uplift 18/05/-17/07/2020. Due to the 6-day revisit time of Sentinel1A/1B acquisitions, the exact timing of inflation/deflation episodes may be shifted by a few days. The time-series analysis was carried out using the Small Baseline Subset (SBAS) algorithm[39], implemented in SARscape, which is based on the combination of interferograms characterized by small, normal and temporal baselines, maximizing spatial and temporal coherence and therefore the quality of the interferograms (maximum temporal baseline 18 days), resampling with a multi-look of 7:2 for range and azimuth direction, respectively (Goldstein filter[40] window size of 32 pixels, coherence threshold of 0.2, ground resolution of 30 m). The topographic phase contribution was subtracted using the ArcticDEM digital terrain model of 2 m spatial resolution. InSAR time-series were compared to data from a GNSS station provided by the IMO and available through the University of Iceland[41], showing good agreement for both ascending and descending datasets (**Ext. data Figs. 3a & 3b**). Ascending and descending LOS displacement maps were combined to derive the vertical and the E-W components of the ground motion (**Ext. data Figs. 3c & 3d**).

Gravity data processing

Each of the four gravity campaigns (**Ext. data Fig. 5 & Tab. S1**) lasted for a few days. Elevation and gravity at the second to northernmost station (HS22) were used as a reference (**Ext. data Fig. 4**), but free-air corrected by up to 2.6 μGal to account for small elevation changes at this site between campaigns. The gravity value at the northernmost and westernmost stations (HS16 and SNH25) were less constrained or had difficult local conditions due to snow and ice and were therefore regarded as unreliable. Finally, the gravity data were corrected for tidal and latitude effects and free-air gravity computed using elevation changes obtained from InSAR measurements. The data were not corrected for ocean tides, as these effects can be considered negligible.

The uncertainty in similar gravity campaigns is generally 10-15 μGal for individual data points. However, these error limits are highly dependent on external conditions such as weather prior to and during the measurements, local site conditions, nearby anthropogenic activity, or seismic noise. We selected only quiet and calm days to minimize the measurement uncertainty. Our dataset provides consistent maximum values close to the centre of uplift which decrease with distance from the centre. However, a few data points are outliers, both with respect to the general trend with time and the nearby stations. Apart from obvious outliers, we estimate, based on the internal consistency of the data, that the error limits are close to ±5 μGal.

We corrected for long-term background gravity reduction caused by the net production of geothermal fluid at Svartsengi[42]. The ratio of the total gravity decrease from 1976 to 2014 to the corresponding net mass production gives a gravity decrease of $0.67 \cdot 10^{-9}$ μGal/kg. By applying this to the estimated production of 2020 we get a value of 5.1 μGal/year at the centre of uplift.

Joint DAS and seismic network processing

The DAS strain-rate data were recorded using a Silixa iDAS (version 2) interrogator with a sampling frequency of 1 kHz, a gauge length of 10 m and a spatial channel offset of 4 m along the full length of the fibre. The DAS data have been included as 40 virtual single-component stations by extracting the DAS signal at regular 500 m intervals along the fibre. For each virtual station, the signal was integrated over 36 m (9 channels) along the cable to improve the signal to noise ratio.

The employed automatic detection method[43] is based on an image function (IF) computed for a grid of potential source positions and times. The IF is computed from the stacking of time-back-shifted waveform attributes of P- and S-phases using the local velocity model (**Tab. S3**). Waveform attributes of P-phases employ a smoothed STA/LTA function[43] calculated from filtered seismograms (3-25 Hz). S-phase attributes are calculated from a smoothed squared signal, which is more sensitive to high amplitudes. Smoothing causes the detector to be more robust against errors in the assumed seismic velocities and reduces the computational cost. Waveform attributes are normalized by a moving average with a duration longer than a typical transient event. Seismic events appear as spatio-temporal peaks in the 4D image function. A detection is registered when the IF exceeds a certain threshold value. The position of the spatio-temporal peak is used to provide the origin time and location. The detector is implemented in the Lassie software package, distributed under the Pyrocko framework[44] (**Tab. S2**).

Poroelastic modelling

The poroelastic model uses the semi-analytical tool POEL[30], which simulates strongly coupled diffusion-deformation processes induced by injection (pumping) tests. Based on Biot's poroelasticity theory, a poroelastic medium can be defined with 5 parameters; the shear rigidity μ, the drained Poisson's ratio ν, the undrained Poisson's ratio ν_u, the Skempton coefficient B and the hydraulic diffusivity D. We adopt the seismic reference model SIL (**Suppl. Information Tab. S3**)[45]. As the diffusion effect might be negligible in the seismic frequency band, μ and v_u can be derived simply from the density and seismic velocities (**Suppl. Information Tab. S3**). Except for a thin permeable aquifer layer representing the medium saturated with compressible fluid, which is inserted into the layered half-space at the depth z, all other layers are assumed to be nearly impermeable ($D \rightarrow 0$). We choose a standard and uniform value for the drained Poisson's ratio ($\nu = 0.25$) of the whole layered structure including the aquifer layer. Note that no diffusion process can happen in the impermeable layers. Therefore, only the elastic property represented by the shear modulus and the undrained Poisson's ratio is relevant for these layers.

Finally, there are only 4 free parameters (z, μ, B and D) characterizing the aquifer layer. We optimize all these parameters so that the predicted surface deformation best fits the InSAR data. Note that the thickness of the aquifer (here 10 m) is rather arbitrary, as the surface deformation is not independently influenced by the thickness and hydraulic diffusivity, but by their product determining the aquifer transmissivity.

The source is represented by episodic fluid injections into the thin and vertically confined aquifer. The central location of injection coincides with the maximum surface uplift at 63.870°N/22.465°W. Each of the 3 uplift episodes is attributed to a constant injection rate. The timings of injection are estimated directly by the uplift-subsidence turning points of the

InSAR time series with a resolution of 6 days; Episode 1 from day 12 to 42, Episode 2 from day 60 to 108, and Episode 3 from day 132 to 192 in 2020. The surface uplift exhibits a slightly elliptic pattern, which can be interpreted as preferential diffusion of intruded fluid along the main strike of fracture systems under the Svartsengi HT field (**Ext. data Fig. 1**). For this purpose, we use a Gaussian line source instead of a point source. The source line orientation and its characteristic length are optimized, too. Note that the surface deformation is related linearly with the 3 constant intrusion rates, but non-linearly with the aquifer parameters and the source geometry. We optimize all these nonlinear parameters by a trial-and-error approach. For each candidate set of nonlinear parameters, we estimate the 3 intrusion rates by the least-squares method. The final optimal model has the minimum misfit between the predicted and observed surface deformation derived from 139 pairs of ascending and descending InSAR images.

An optimal choice of the parameter set is given by $z = 4.0$ km, $\mu = 7.55$ GPa, and $D = 0.10$ m^2/s (for the aquifer thickness fixed at 10 m). The line source has a characteristic length of 4.0 km (two sigma of the Gaussian distribution) and is oriented to N60°E. The normalized variance of misfits between the predicted and observed InSAR data is about 5%. The surface subsidence after each uplift episode is successfully explained by relaxation of the intrusion-induced overpressure through fluid diffusion within the aquifer.

In comparison, the aquifer depth and the source geometry are well resolved and consistent with those obtained from the Mogi and rectangle dislocation models. However, there is a certain trade-off between μ and D. The InSAR data can be explained equally well using any combination of the two parameters within a roughly elliptical trade-off zone covering about $0.1 \leq \mu/\mu_s \leq 0.8$ and $0.03 \leq D \leq 0.12$ m^2/s (**Suppl. Information sheet Fig. IS3-1**), where $\mu_s = 15.1\,\mathrm{GPa}$ is the shear modulus of the top elastic layer above the aquifer. The estimated fluid intrusion volume is mainly controlled by B, but it can also be slightly affected by about ±5% through different choices of the μ-D combination, e.g., 40±2 x 10^6 m^3 for B = 0.3 (**Suppl. Information sheet Fig. IS3-2**). In fact, when fixing all other parameters, the same surface deformation can be produced using different B values if the intruded volume remains proportional to B^{-1}.

For the quasi-static poroelastic deformation, only the volume of intruded fluid, rather than its mass, is relevant. The latter can only be constrained by the gravity data in the present study. It is known that the internal deformation has no effect on the free-air gravity change for spherical pressure sources in a homogeneous half-space[46]. Based on this, and on predictions from superposition of spherical pores[47], we infer that the effect of internal deformation is still negligible in comparison to the primary effect of the intruded mass on the free-air gravity. Thus, we use the POEL output for Darcy flux to calculate the spatio-temporal redistribution of the intruded mass within the aquifer and its contribution to the free-air gravity change on the surface. A simple comparison between the predicted and observed free-air gravity anomalies yields an estimate of intruded fluid mass of about 82 Mt. The misfits of the model predictions to the gravity data are all within the measurement uncertainties of about ±5 μGal (**Ext. data Fig. 5**). In the present case, a realistic estimate of the Skempton coefficient is given by $0.08 \leq B \leq 0.19$ (**Ext. data Fig. 9 & Suppl. Information sheet IS3**). Accordingly, the intruded volume varying between 0.068-0.161 km^3, the density of the intruded fluid is estimated to be between 500-1200 kg/m^3.

Seismicity modelling

We applied the Coulomb-Rate-and-State model, widely used for natural, anthropogenic, and volcanic activity[32,48,49,50,51]. In this model, the earthquake rate as a function of space $\vec{x}$ and time t is given by:

$R(\vec{x},t) = \frac{r(\vec{x})}{\dot{\tau}\gamma(\vec{x},t)}$,

where r is the background seismicity rate, $\dot{\tau}$ is the background shear stressing rate, and γ is a state variable. The evolution of γ depends on the stress history at the given location $\vec{x}$, the background stressing rate $\dot{\tau}$, and the product $A{\cdot}\sigma$, where A is a constitutive parameter related to the direct effect in the laboratory-derived rate-and-state friction law and σ is the effective normal stress acting on the faults. Since neither A nor σ are well-constrained for natural faults, the product $A{\cdot}\sigma$ is usually considered as a free parameter. Fits to various seismic sequences yielded $A{\cdot}\sigma$-values between 0.01 and 0.1 MPa[51].

We estimated the CFS stress history by_$\tau_{max}(\vec{x},t) + f \cdot p(\vec{x},t)$, where f is the friction coefficient typically in the range from 0.1 to 0.8, and τ_{max} and p are the induced maximum shear and pore pressure. Here, we use the maximum shear value to account for variable receiver mechanisms of the small to moderate magnitude earthquakes. We find that f only slightly affects the results and set it to f=0.7. Based on the geodetically constrained poroelastic model described above, we calculated CFS using the POEL code at grid points $\vec{x}$ in a spatial box with a dimension of 30 km in the NS- and 60 km in the EW-direction, centred at the deformation source, and at six depth levels up to 3 km, with a grid spacing of 0.5 km.

The background rate $r(\vec{x})$ and the background stressing rate $\dot{\tau}$ were estimated by preceding seismicity. For that purpose, we analysed the earthquakes in the IMO-catalogue that occurred in this region between 2000 and the end of 2019. The catalogue is complete for M≥1.5 during this period, while it is complete for M≥1.0 in 2020. The rate of M≥1.5 background events in the selected region is found to be r = 0.76 days^{-1}, which translates to r = 2.41 M≥1 events days^{-1}

assuming a Gutenberg-Richter magnitude distribution with b=1. The spatial distribution of $r(\vec{x})$ is estimated by laterally smoothing the epicentres using a Gaussian filter with a standard deviation of 1 km and assuming a uniform distribution at depth. The uniform stressing rate $\dot{\tau}$ is estimated using Kostrov's formula for our selected region[52,53], assuming a maximum earthquake magnitude of M6 and an effective thickness of the seismogenic zone of 4 km, resulting in $\dot{\tau}$= 12 Pa/day.

The single free model parameter $A\cdot\sigma$, determining the strength of the seismic activation due to the stress changes, is set by matching the total observed number of earthquakes, yielding $A\cdot\sigma$ = 0.02 MPa, which is well within the range of previously observed values. The spatio-temporal fits of the final model are presented in **Fig. 3** for earthquakes above the completeness magnitude of M1.0 in 2020.

Cyclic fluid transport modelling of magmatic volatiles

The buoyancy-driven drainage of a deep reservoir by viscous channel flow resembles gravity-driven outflow from a tank through a pipe. If viscosity is dominant, the flux follows an exponential decay with $q(t) = q_0\ e^{-t/t0}$, where q_0 is the initial flux at time t=0 with $t_0 = \pi\cdot r^2\cdot h_2(t=0)/q_0$ (**Fig. 5a & Suppl. Information sheet IS1**). The ascent height h or the length L of the inclined channel do not enter the problem. The modelling of the total influx after three uplift episodes leads to a draining decay time of t_0 = 95 days and an initial flux of q_0 = 4.1 m^3/s (**Fig. 5b**).

The cyclic ascent of finite-volume fluid batches can be explained by buoyancy-driven fracture movement. The fluid flux rate, q(t), controls the filling of batches. The ascent of a fracture through a channel and the detachment from the feeding system below is controlled by the stress intensity at the upper and lower tip of the fracture[54]. The intrusion batches arrive at the sealed aquifer at 4 km depth with estimated volumes of ~$45\cdot10^6$ m^3, ~$38\cdot10^6$ m^3 and ~$27\cdot10^6$

m^3 for the first, second, and third batch, respectively (**Fig. 5b**). The ascent velocity of the fluid batch depends on several factors, including the properties of the channel, the alteration of rocks[36] and the enclosed fluid volume controlling the internal overpressure[54]. A constant ascent velocity is supported by laboratory experiments of finite volume fluid ascent in gelatine[54].

The fracture model explains the injected volumes and the onset and inter-event time of the three uplift cycles (**Fig. 5b & c**). The fit has been obtained by matching the accumulated volume at the end of phase 3, $\Sigma V = V_1+V_2+V_3$, and the onset of the first injection phase. The model is also consistent with the onsets of uplift phases 2 and 3 and perhaps a fourth phase at Krýsuvík in August 2020 (**Figs. 5c & 6, Ext. data Fig. 8**). The model cannot resolve the ascent times of the fluid batch to the injection point at the aquifer at 4 km depth. The onset of an uplift phase in **Fig. 5b** and **c** represents the arrival time at 4 km depth. In contrast, the filling of the first fluid batch is estimated for the December 18th, 2019 (**Fig. 5c**), which correlates with the occurrence of the strong earthquake swarm on December 15th-20th, 2019, at 5-6 km depth and about 7 km east of the centre of uplift. We speculate that the inflow traversed from this location. This would also link the unrest beneath Svartsengi to the eruption that started in March 2021 just above the location of the December 2019 earthquake swarms (**Ext. data Fig. 6**). The increasing duration of the injection into the aquifer may imply that the pressure difference between the injection source and the sealed aquifer decreased with the arrival of each new over-pressurized batch.

Data availability

The basic data used in this paper consist of InSAR, seismic and gravity data.

InSAR data: The radar data acquired by the Copernicus Sentinel-1A and 1B satellites are available at no cost from the European Space Agency's Copernicus Open Access Hub (https://scihub.copernicus.eu/) and can be interferometrically processed using the freely available Sentinel 1 toolbox (https://step.esa.int/main/toolboxes/sentinel-1-toolbox/). The InSAR data generated from the Copernicus Sentinel-1A and 1B satellites and as published in the paper are available on Zenodo, https://zenodo.org/record/6344933, or https://doi.org/10.5281/zenodo.6344933

Seismic data: The earthquake catalogue based on waveform stacking from DAS and local seismic stations presented in this paper is available on Zenodo, https://zenodo.org/record/6337788 , DOI: https://doi.org/10.5281/zenodo.6337788 .

Seismic data from the permanent national seismic network in Iceland are available from the open database of the Iceland Met Office, https://skjalftalisa.vedur.is
For data from temporary stations from the Czech Academy of Sciences, Czech Republic, restrictions apply to the availability, which were used under licence for the current study, and so are not publicly available. These data are however available from the authors upon reasonable request and with permission of the Czech Academy of Sciences.
The seismological data from temporary GFZ stations analysed during the current study are available in the GEOFON repository at https://geofon.gfz-potsdam.de/waveform/archive under code 9H and Dahm, T., Jousset, P., Heimann, S., Milkereit, C., Hersir, G.P., Magnússon, R. (2020): MAGIC - Seismic network MAGma in Iceland, https://doi.org/10.14470/4U7575229166 (restricted until 01/2026).
Seismological waveform data from the glass-fibre cable monitoring in SW Reykjanes Peninsula are available from the GEOFON data centre, under network code 5J. This dataset

comprises a selection of waveforms recorded along an optical fibre of 21 km length. The subset consists of 40 channels at 100 Hz (spatially stacked 9x). Specific full data set is available upon request to the authors. Jousset, P., Hersir, G.P., Krawczyk, C., Wollin, C., Lipus, M., Reinsch, T., Isken, M., Heimann, S. (2020): MAGIC (MAGma in Iceland). GFZ Data Services. Other/Seismic Network. DOI: https://doi.org/10.14470/0W7575244885 .
The preliminary seismic catalogue used in this study has been derived by combining horizontal strain DAS and local seismic stations in a migration-based detection and location approach using the open-source Lassie software (https://git.pyrocko.org/pyrocko/lassie/).

The gravity data are available on Zenodo: https://zenodo.org/record/6344613 and DOI 10.5281/zenodo.6344613

All other data generated or analysed during this study are included in this published article and its supplementary information files in form of tables, or available from the corresponding author on reasonable request.
All general request regarding the paper, the geological interpretation, the conceptual model, and the gravity data should be directed to the corresponding author, Ólafur G. Flóvenz, ÍSOR, Iceland GeoSurvey, ogf@isor.is
Requests regarding other specific parts of the paper should be directed as follows:
Seismic data processing and interpretation: Sebastian Hainzl, hainzl@gfz-potsdam.de
Poroelastic modelling: Rongjiang Wang, wang@gfz-potsdam.de
InSAR data processing and modelling: Thomas Walter, twalter@gfz-potsdam.de
Cyclic fluid transport modelling: Torsten Dahm, dahm@gfz-potsdam.de

Code availability

The seismic recordings were processed with Pyrocko [44]. The software package Lassie (https://git.pyrocko.org/pyrocko/lassie.git) was used for detection and localisation of earth-quakes.

Recorded DAS data was converted using iDAS Convert (Isken, M., Wollin, C., Heimann, S., Quinteros, J., Jäckel, K.-H., Jousset, P. (2021). DAS Convert - Convert distributed acoustic sensing data. V. 1.0. GFZ Data Services. https://doi.org/10.5880/GFZ.2.1.2021.005). The seismic software frameworks are publicly available at https://pyrocko.org. The seismic software code is open, and methods have been reviewed publicly.

Method References

39. Berardino, P., Fornaro, G., Lanari, R. & Sansosti, E. A new algorithm for surface deformation monitoring based on small baseline differential SAR interferograms. *IEEE Transactions on Geoscience and Remote Sensing* **40**, 2375–2383 (2002).
40. Goldstein, R.M. & Werner, C.L. Radar interferogram filtering for geophysical applications. *Geophys. Res. Lett.*, **25**, 4035–4038 (1998).
41. Institute of Earth Sciences, University of Iceland. https://notendur.hi.is/~hgeirs/iceland_gps/icel_400p.html.
42. Orkustofnun. https://orkustofnun.is/gogn/Talnaefni/OS-2020-T009-01.pdf (2020).
43. Allen, R.V. Automatic earthquake recognition and timing from single traces. *Bull. Seism. Soc. Am*. **68**, 1521-1532 (1978).
44. Heimann, S. et al. Pyrocko - An open-source seismology toolbox and library. V. 0.3. GFZ Data Services. https://doi.org/10.5880/GFZ.2.1.2017.001 (2017).
45. Stefánsson, R. et al. Earthquake prediction research in the South Iceland seismic zone and the SIL project. *Bull. Seism. Soc. Am*., **83** (3), 696-716 (1993).
46. Walsh, J.B. & Rice, J.R. Local changes in gravity resulting from deformation, *J. Geophys. Res.,* **84**, 165 – 170, doi.org/10.1029/JB084iB01p00165 (1979).

47. Amoruso, A. & Crescentini, L. Shape and volume change of pressurized ellipsoidal cavities from deformation and seismic data. *J. Geophys. Res.: Solid Earth*, **114.B2**, https://doi.org/10.1029/2008JB005946 (2009).

48. Dieterich, J., Cayol, V. & Okubo, P. The use of earthquake rate changes as a stress meter at Kilauea volcano. *Nature* **408**, 457-460 (2000).

49. Heimisson, E.R. & Segall, P. Physically consistent modeling of dike-induced deformation and seismicity: Application to the 2014 Bàrðarbunga dike, Iceland. *J. Geophys. Res*., **125**, e2019JB018141. https://doi.org/10.1029/2019JB018141

50. Toda S., Stein, R.S. & Sagiya, T. Evidence from the AD 2000 Izu islands earthquake swarm that stressing rate governs seismicity. *Nature* **419**, 58-61.

51. Hainzl, S., Steacy, S. & Marsan, D. Seismicity models based on Coulomb stress calculations. Community Online Resource for Statistical Seismicity Analysis (2010). https://doi.org/10.5078/corssa-32035809. [Available at http://www.corssa.org.].

52. Kostrov, B. Seismic moment and energy of earthquakes, and seismic flow of rock, Izv. Acad. Sci. *USSR Phys. Solid Earth*, **1**, 23-40 (1974).

53. Dahm, T., Cesca, S., Hainzl, S., Braun, T. & Krüger, F. Discrimination between induced, triggered, and natural earthquakes close to hydro-carbon reservoirs: A probabilistic approach based on the modeling of depletion-induced stress changes and seismological source parameters, *J. Geophys. Res*., **120**, 2491-2509 (2015). doi:10.1002/2014JB011778.

54. Dahm, T. On the shape and velocity of fluid-filled fractures in the Earth. *Geophys. J. Int.* **142**, 181-192 (2000).

55. Karlsdóttir, R. TEM-viðnámsmælingar í Svartsengi 1997. Orkustofnun, OS-98025, 43 (1998).

56. Ducrocq, C. et al. Inflation-Deflation Episodes in the Hengill and Hrómundartindur Volcanic Complexes, SW Iceland. *Front. Earth Sci*. 9:725109. doi: 10.3389/feart.2021.725109, (2021).

818

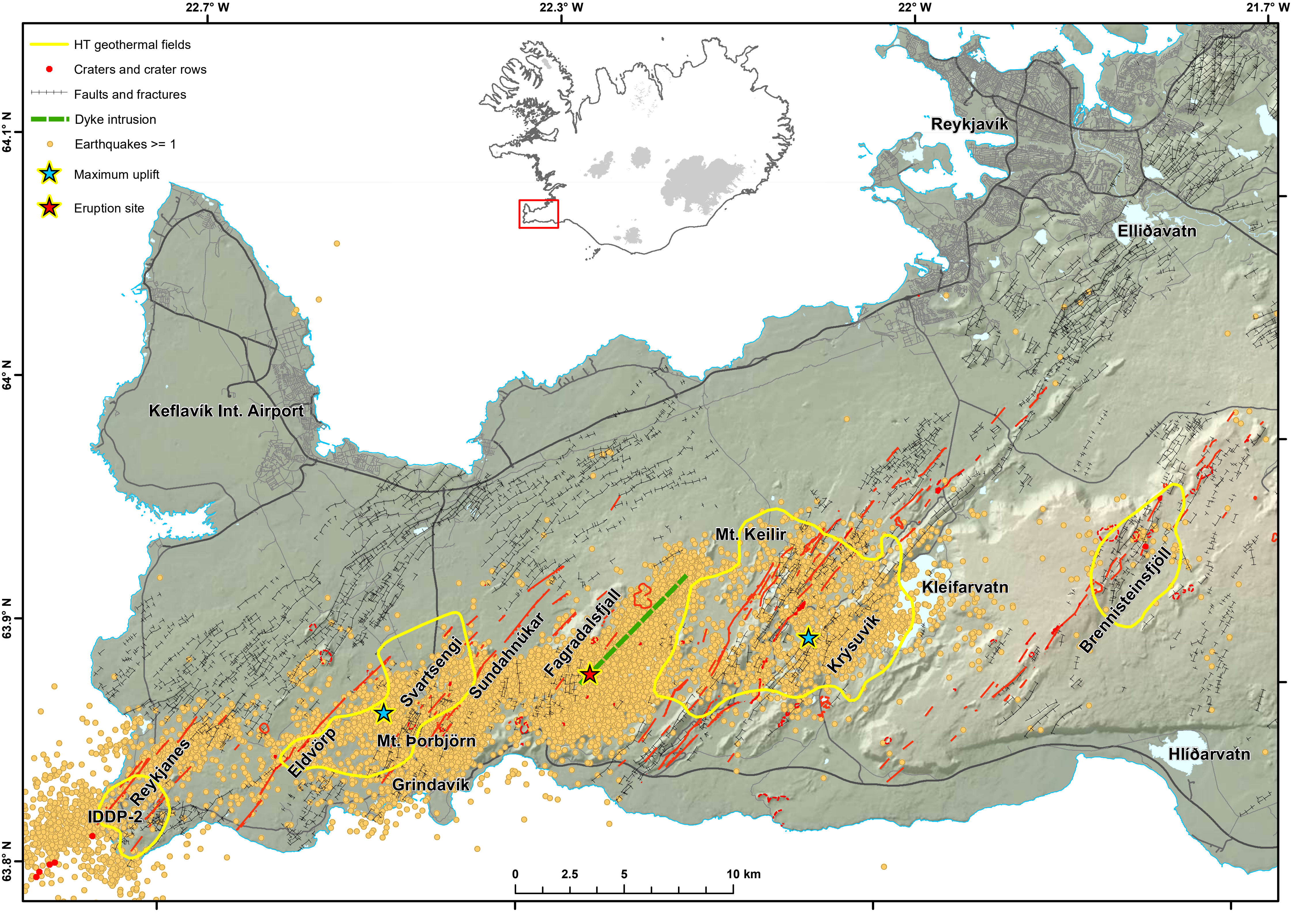

22.7° W
22.3° W
22° W
21.7° W
64.1° N
64° N
63.9° N
63.8° N
HT geothermal fields
Craters and crater rows
Faults and fractures
Dyke intrusion
Earthquakes >= 1
Maximum uplift
Eruption site
Reykjavík
Elliðavatn
Keflavík Int. Airport
Mt. Keilir
Kleifarvatn
Brennisteinsfjöll
Krýsuvík
Fagradalsfjall
Sundahnúkar
Svartsengi
Eldvörp
Mt. Þorbjörn
Grindavík
Reykjanes
IDDP-2
Hlíðarvatn
0
2.5
5
10 km

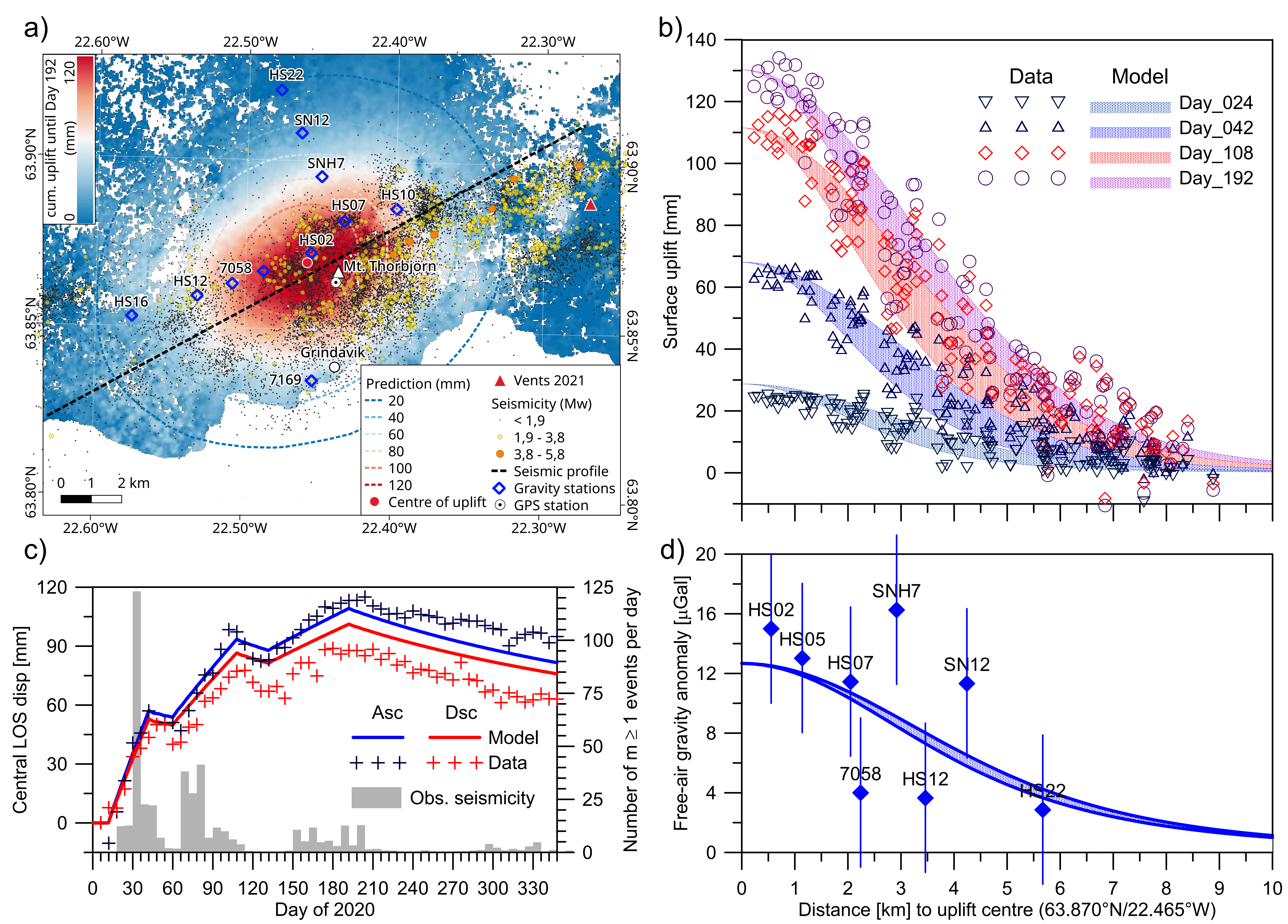

a)
22.60°W
22.50°W
22.40°W
22.30°W
63.90°N
63.85°N
63.80°N
cum. uplift until Day 192 (mm)
0
120
HS22
SN12
SNH7
HS10
HS07
HS02
Mt. Thorbjorn
7058
HS12
HS16
Grindavik
7169
0 1 2 km
Prediction (mm)
20
40
60
80
100
120
Centre of uplift
Vents 2021
Seismicity (Mw)
< 1,9
1,9 - 3,8
3,8 - 5,8
Seismic profile
Gravity stations
GPS station
b)
Surface uplift [mm]
Data
Model
Day_024
Day_042
Day_108
Day_192
c)
Central LOS disp [mm]
Number of m ≥ 1 events per day
Day of 2020
Asc
Dsc
Model
Data
Obs. seismicity
d)
Free-air gravity anomaly [µGal]
HS02
HS05
HS07
SNH7
SN12
7058
HS12
HS22
Distance [km] to uplift centre (63.870°N/22.465°W)

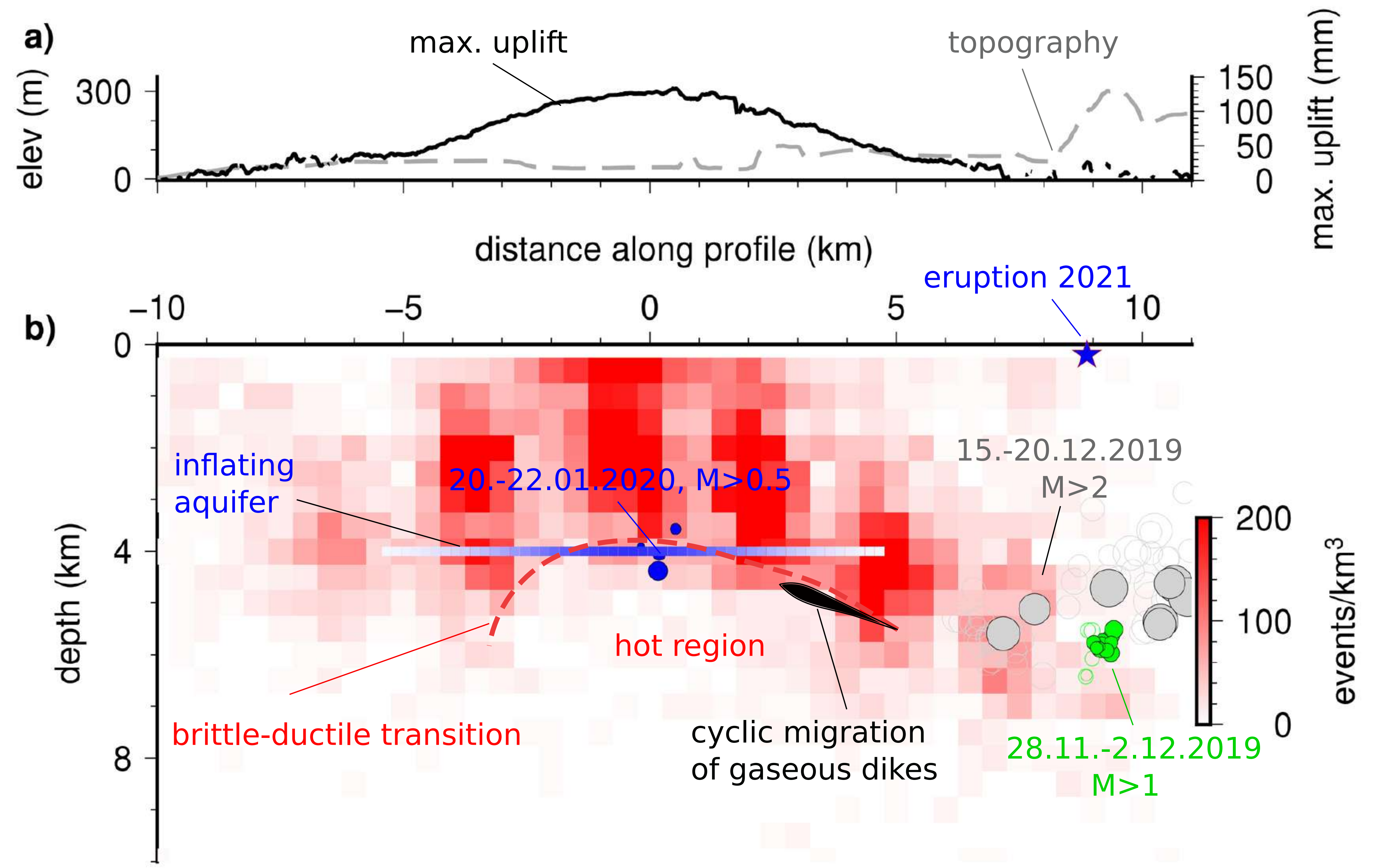

a)
max. uplift
topography
elev (m)
300
0
150
100
50
0
max. uplift (mm)
distance along profile (km)
eruption 2021
–10
–5
0
5
10
b)
0
4
8
depth (km)
inflating
aquifer
20.-22.01.2020, M>0.5
15.-20.12.2019
M>2
200
100
0
events/km^3
hot region
brittle-ductile transition
cyclic migration
of gaseous dikes
28.11.-2.12.2019
M>1

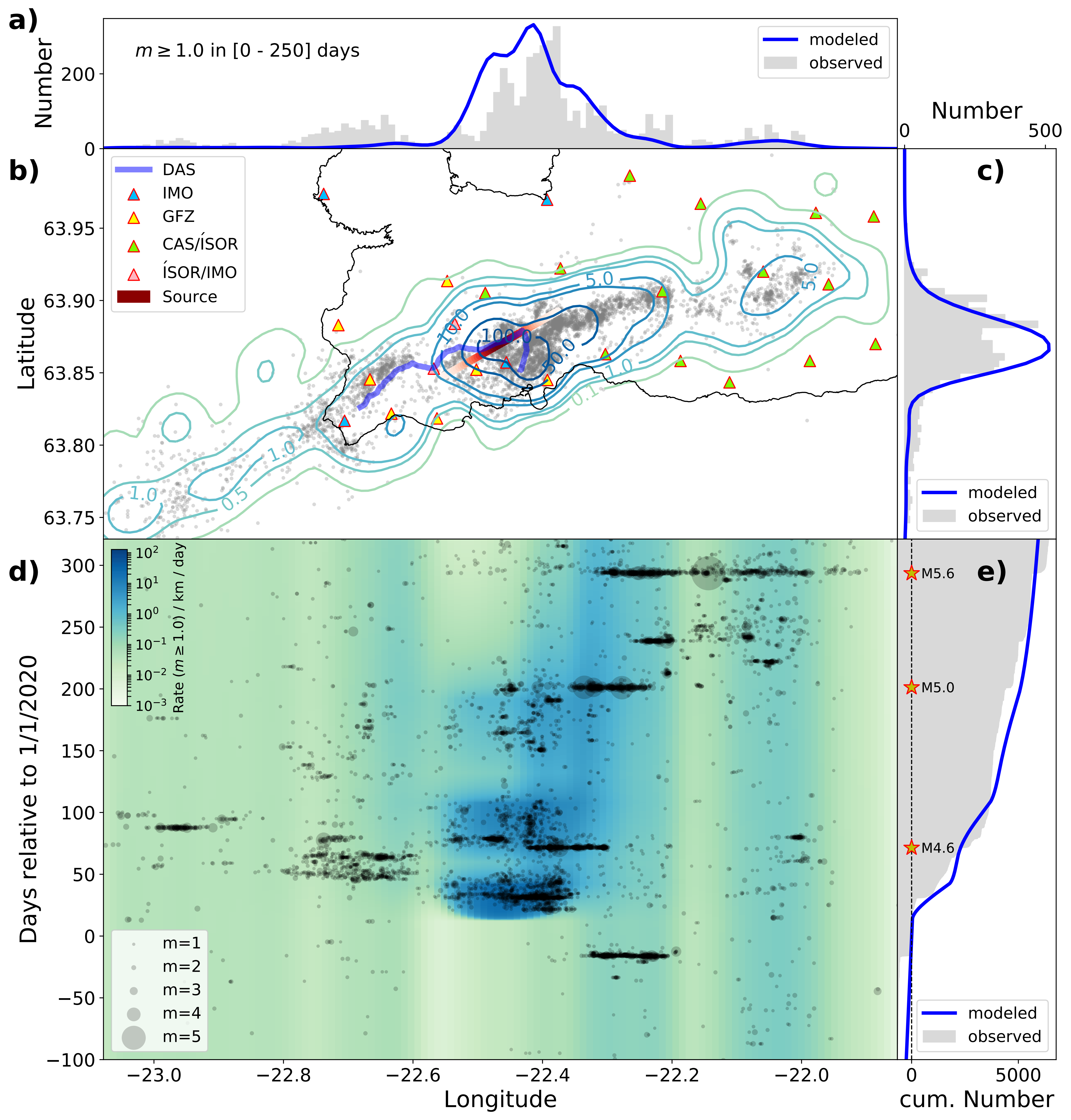

a)
b)
c)
d)
e)
$m \geq 1.0$ in [0 - 250] days
Number
modeled
observed
DAS
IMO
GFZ
CAS/ÍSOR
ÍSOR/IMO
Source
Latitude
Longitude
Days relative to 1/1/2020
Rate ($m \geq 1.0$) / km / day
m=1
m=2
m=3
m=4
m=5
M5.6
M5.0
M4.6
cum. Number

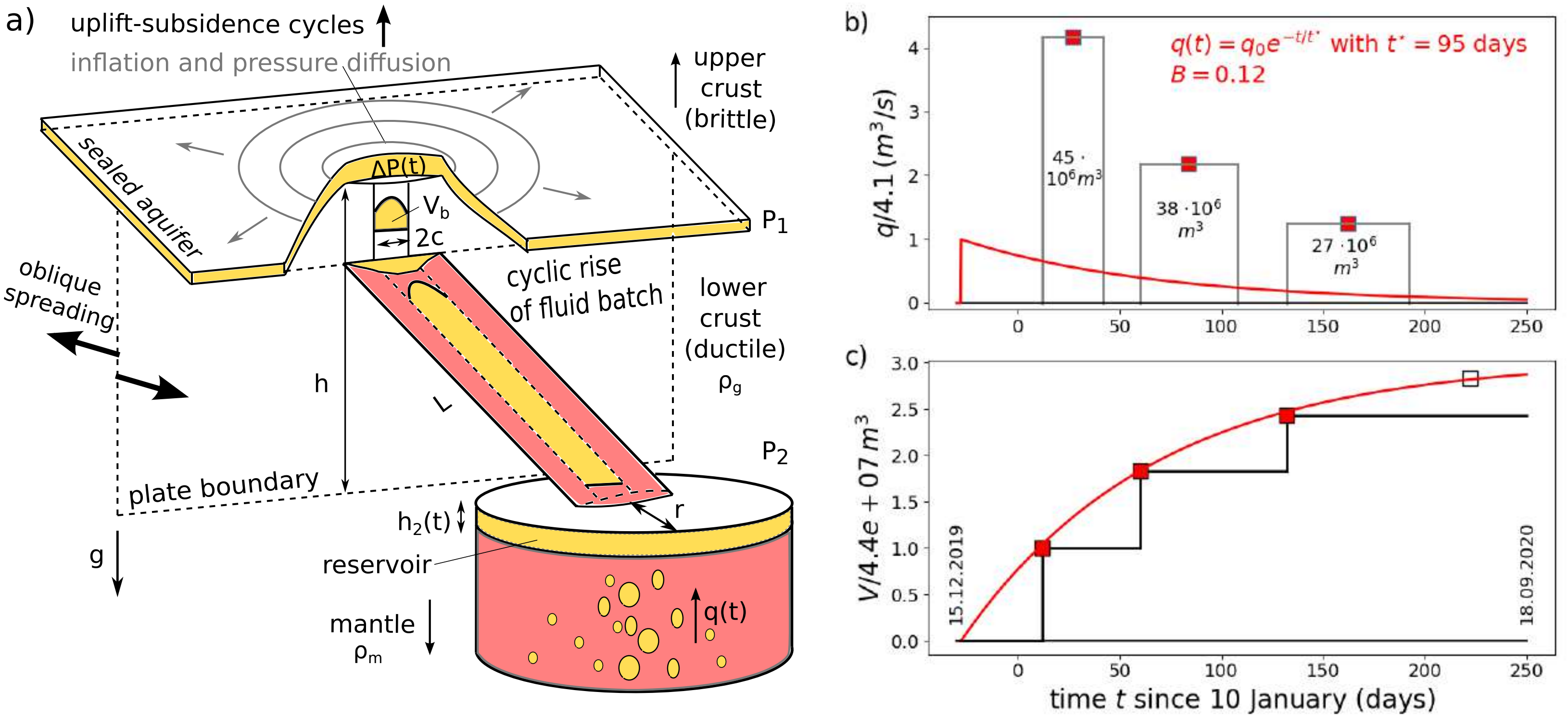

a)
uplift-subsidence cycles
inflation and pressure diffusion
upper crust (brittle)
sealed aquifer
ΔP(t)
V_b
2c
P_1
oblique spreading
cyclic rise of fluid batch
lower crust (ductile)
ρ_g
h
L
P_2
plate boundary
$h_2(t)$
r
g
reservoir
q(t)
mantle
ρ_m
b)
$q(t) = q_0 e^{-t/t^*}$ with $t^* = 95$ days
$B = 0.12$
$q/4.1\ (m^3/s)$
$45 \cdot 10^6 m^3$
$38 \cdot 10^6 m^3$
$27 \cdot 10^6 m^3$
c)
$V/4.4e+07\ m^3$
15.12.2019
18.09.2020
time t since 10 January (days)

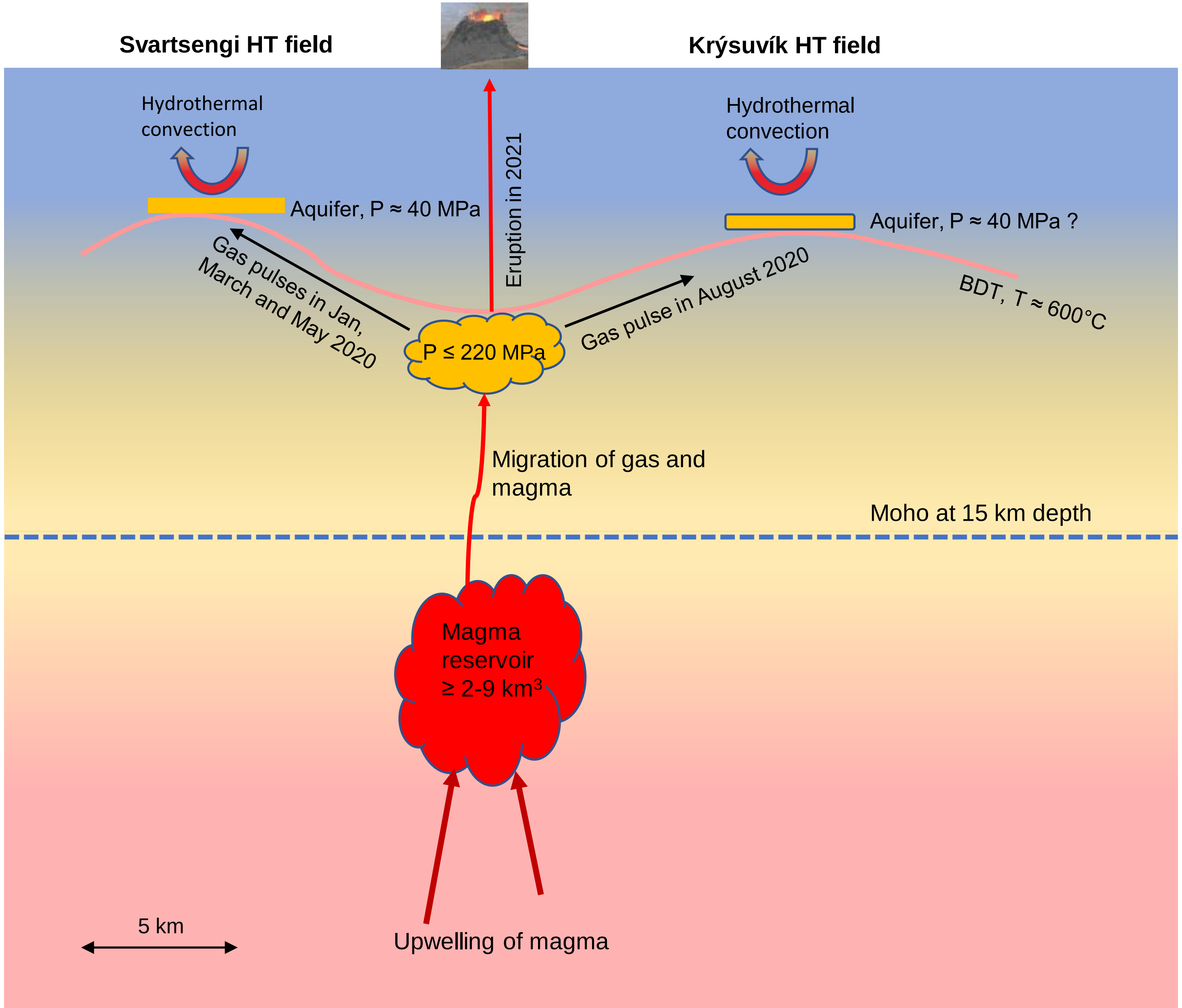

Svartsengi HT field
Krýsuvík HT field
Hydrothermal convection
Hydrothermal convection
Aquifer, P ≈ 40 MPa
Eruption in 2021
Aquifer, P ≈ 40 MPa ?
Gas pulses in Jan, March and May 2020
Gas pulse in August 2020
BDT, T ≈ 600°C
P ≤ 220 MPa
Migration of gas and magma
Moho at 15 km depth
Magma reservoir ≥ 2-9 km³
5 km
Upwelling of magma


22.5° W
22.4° W
63.9° N
63.85° N
Svartsengi
Blue Lagoon
Production wells
Mt. Þorbjörn
Injection wells
Eldvörp
Grindavík
Deep aquifer
Iso-resistivity at 1000 m
Iso-resistivity at 500 m
Geothermal wells
Craters and crater rows
Faults and fractures
Maximum uplift
M4.1 earthquake
0 0.5 1 2 km


InSAR Ascending 20/01/2020 -24/07/2020
InSAR Descending 18/01/2020 -22/07/2020
22.6°W
22.4°W
22.2°W
22.0°W
64.0°N
63.9°N
63.8°N


a
b
c
d
LOS disp. (mm)
vertical disp. (mm)
ascending
GPS asc
descending
GPS desc
vertical
earthquake
2020-01
2020-03
2020-05
2020-07
2020-09
2020-11
2021-01


22.7° W
22.3° W
22° W
64.1° N
64° N
63.9° N
63.8° N
IMO
GFZ
CAS / ÍSOR
ÍSOR / IMO
Maximum uplift
Eruption site
Gravity stations
Fiber optic cable
Craters and crater rows
Dyke intrusion
Reykjavík
Elliðavatn
Keflavík Int. Airport
NYL
VOG
STH
ASH
KAS
LHL
HRG
SNH25
Mt. Keilir
HS22
STF
LSF
SN12
LAG
Fagradalsfjall
FAF
Sveifluháls
MOH
Kleifarvatn
KLV
Brennisteinsfjöll
SNH7
Svartsengi
HS10
HS07
HAS
LFE
Núpshlíðarháls
Krýsuvík
HS02
HS05
7058
Eldvörp
HS12
Mt. Þorbjörn
HS16
RAH
SUH
GRV
KRI
ISS
LAT
ELB
HDV
SYRN
Grindavík
HOP
7169
SEA
Reykjanes
RNE
SDV
BER
0
2.5
5
10 km

a)
27.01. - 20.04.2020
Data
Model
HS02
HS05
HS07
SNH7
SN12
7058
HS12
HS22
Free-air gravity anomaly [µGal]
Distance to center [km]
b)
20.04 - 05.10.2020
7058
SN12
HS22
HS16
HS02
HS05
HS07
7169
Free-air gravity anomaly [µGal]
Distance to center [km]
c)
05.10.2020 - 28.02.2021
HS07
SNH7
7169
HS22
HS16
SN12
HS02
HS05
7058
Free-air gravity anomaly [µGal]
Distance to center [km]
d)
Central free-air gravity anomaly [µGal]
Central uplift [mm]
Days since 01.01.2020

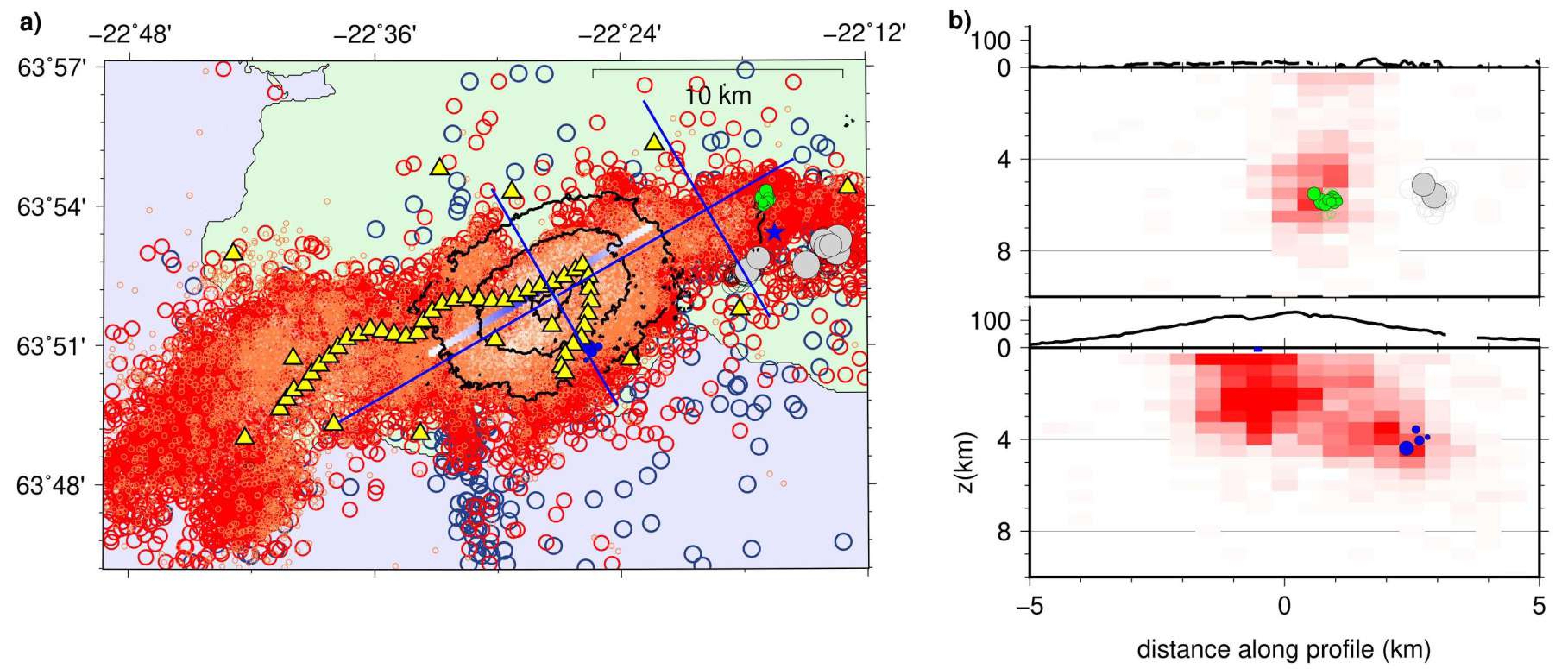
a)
−22˚48'
−22˚36'
−22˚24'
−22˚12'
63˚57'
63˚54'
63˚51'
63˚48'
10 km
b)
100
0
4
8
z(km)
−5
0
5
distance along profile (km)

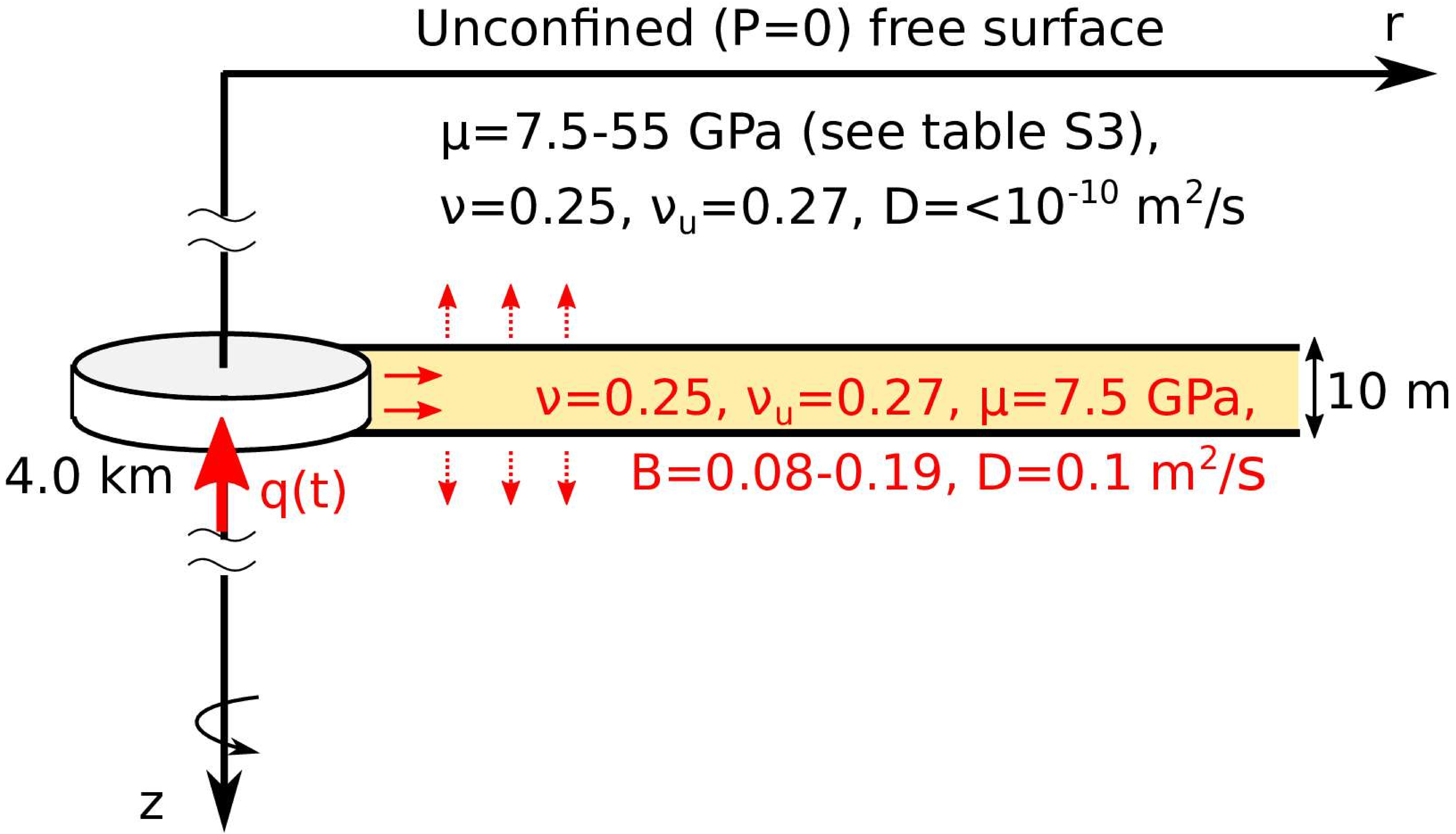

Unconfined (P=0) free surface
r
μ=7.5-55 GPa (see table S3),
ν=0.25, ν_u=0.27, D=<10^{-10} m^2/s
ν=0.25, ν_u=0.27, μ=7.5 GPa,
B=0.08-0.19, D=0.1 m^2/s
10 m
4.0 km
q(t)
z

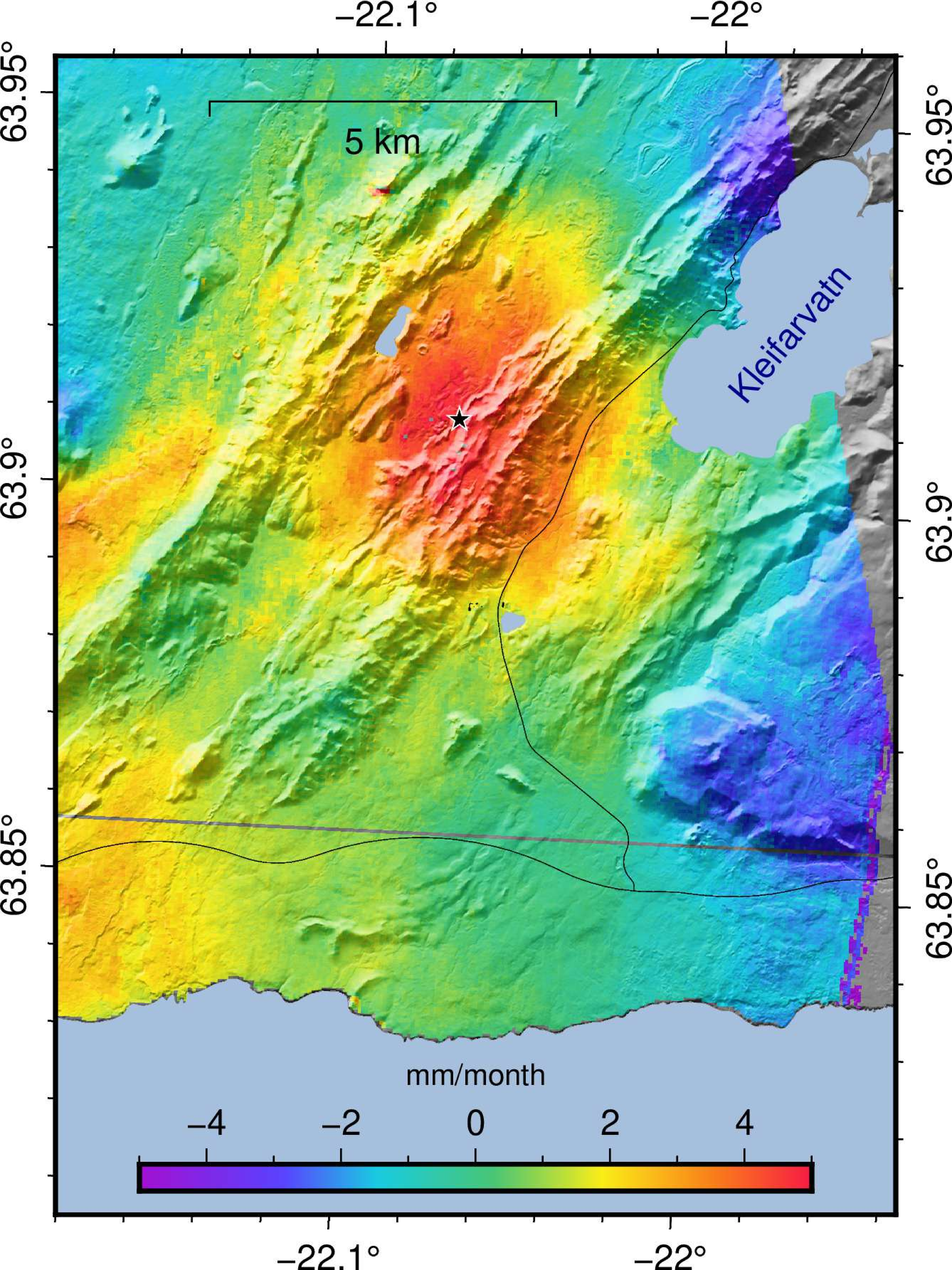

−22.1°
−22°
63.95°
63.9°
63.85°
5 km
Kleifarvatn
mm/month
−4
−2
0
2
4

Fluid density [10³ kg/m³]
Fluid volume [10⁶ m³]
Skempton coefficient B
Magma
Water
0
1
2
3
4
0
50
100
150
200
250
0
0.1
0.2
0.3
0.4
0.5